minerals

Article

Influence of Key Strata on the Evolution Law of Mining-Induced Stress in the Working Face under Deep and Large-Scale Mining

Jianlin Xie [1], Shan Ning [2,*], Weibing Zhu [2], Xiaozhen Wang [2] and Tao Hou [3]

[1] State Key Laboratory of Coal Exploration and Intelligent Mining, China University of Mining and Technology, Xuzhou 221116, China
[2] School of Mines, China University of Mining and Technology, Xuzhou 221116, China
[3] Shaanxi Zhengtong Coal Industry Co., Ltd., Xianyang 713600, China
* Correspondence: ningshan@cumt.edu.cn

Abstract: When there are multiple key strata in the overburden of a deep coal seam and the surface subsidence coefficient after mining is small, this indicates that the overlying key strata fail to break completely after mining. On this occasion, stress is easily concentrated in the working face, which in turn leads to the occurrence of dynamic disasters such as rock bursts. This study adopted a comprehensive analysis method of field monitoring and numerical simulations to explore the influence of the key stratum on the evolution law of mining-induced stress in the working face. A distributed optical fiber sensor (DOFS) and a surface subsidence GNSS monitoring system were arranged inside and at the mouth of the ground observation borehole, respectively. According to the monitoring results of strain obtained from the DOFS, the height of the broken stratum inside the overlying strata was obtained and according to the monitoring results of surface subsidence, the surface subsidence coefficient was proven to be less than 0.1, indicating that the high key stratum is not broken completely, but enters a state of bending subsidence instead. In order to reveal the influence of the key stratum on the mining-induced stress of the working face, two 3DEC numerical models with and without the key stratum were established for a comparative analysis. As the numerical simulation results show, when there are multiple key strata in the overburden, the stress influence range and the stress concentration coefficient of the coal seam after mining are relatively large. The study revealed the working mechanism of rock burst accidents after large-scale mining and predicted the potential area with a rock burst risk after mining of the working face, which was verified by field investigations. The research results are of great guiding significance for the identification of the working mechanism of rock bursts in deep mining condition and for their prevention and control.

Keywords: key strata; mining-induced stress; DOFS; 3DEC; large-scale mining

Citation: Xie, J.; Ning, S.; Zhu, W.; Wang, X.; Hou, T. Influence of Key Strata on the Evolution Law of Mining-Induced Stress in the Working Face under Deep and Large-Scale Mining. *Minerals* **2023**, *13*, 983. https://doi.org/10.3390/min13070983

Academic Editor: Mamadou Fall

Received: 21 June 2023
Revised: 18 July 2023
Accepted: 21 July 2023
Published: 24 July 2023

1. Introduction

The movement of overlying strata after coal mining will exert some impact on the stress evolution of the underground working face. The key stratum plays a major role in bearing the overlying strata [1]. Accordingly, it is of particular importance to understand the influence of the key stratum distribution in the overlying strata on the evolution of mining-induced stress in the working face.

Mining-induced stress distribution of the working face in a kilometer-deep coal mine has been studied [2]. Different key stratum thicknesses and heights have been numerically simulated by Universal Distinct Element Code (UDEC) software in order to study the effect of key stratum on the mining abutment pressure of a coal seam [3]. The distribution of energy accumulation and fracture positions before and after the fracture of overlying key strata has been derived, and the energy release of fractures in each stratum has been calculated [4]. The mechanism and evolution control of pillar bursts in different thickness key strata have been studied using field investigations, theoretical analysis, and numerical simulation [5]. The spatial fracture characteristic of overlying strata was analyzed by Winkler elastic foundation beam theory [6]. Based on the key strata theory, an overburden caving model was proposed to predict the multilayered hard strata behavior [7]. A new damage model based on the modified thermomechanical continuum constitutive model in coal mass and the contact layers between the rock and coal mass was proposed [8]. A fracture failure analysis of hard and thick key layers and their dynamic response characteristics was analyzed [9]. Strata movement and stress evolution when mining two overlapping panels affected by hard stratum have been studied [10]. An analysis of the distribution characteristics of the primary key stratum in the coal mine revealed the bow-shaped structural characteristics of the overlying thick primary key stratum [11]. The mechanism, prevention measures, and control methods for earthquake disasters typically occurring in mines with thick and hard rock strata were investigated [12]. A simplified mechanical model for the analysis of the dynamic destabilization of the overlying strata during underground mining was constructed [13]. A study investigated the spatiotemporal effect of mining-induced stress fracture–seepage field coupling characterized by a ladder key stratum and a composite aquifer [14]. Wilson's equations for the vertical stress distribution in the vicinity of a single longwall panel after it has been mined have been used in conjunction with finite element modeling to evaluate vertical stresses in the underlying strata [15]. An estimation method for the cover pressure re-establishment distance and pressure distribution in the goaf of longwall coal mines was presented [16]. Gravitational rules were used as the basis for the prognosis of vertical stress distribution in exploited rock masses [17]. To analyze the law of movement and caving of the roof rock stratum, the roof subsidence displacement, rock stratum stress, and rock stratum movement law were analyzed by using the method of particle discrete elements and similar material simulation tests [18]. Based on the analysis of subsidence and the overlying structural characteristics, the influencing factors and the control effect laws of strata movement were investigated [19].

The working faces in Binchang mining area of China are buried nearly a kilometer deep, with a mining height of over 10 m. After coal mining, the surface subsidence is generally small and underground rock burst accidents occur frequently, indicating that the movement law of the overlying strata has a certain particularity. Through field monitoring and numerical simulations, this study explored the strata movement law of the mine after mining and analyzed the influence of the key stratum of overlying strata on the evolution of mining-induced stress in the working face, laying the foundation for revealing the mechanism of rock bursts.

2. Project Overview

The plane layout of the working face in the mine under study is shown in Figure 1. First, the four working faces LW101~LW104 in panel 1 were mined, then LW201~LW 205 in panel 2 were mined successively, then LW302 in panel 3 was mined; and LW 301 in panel 3 was mined finally. This study mainly analyzed the evolution law of mining-induced stress after mining LW204 and LW205 and then LW302 and LW301.

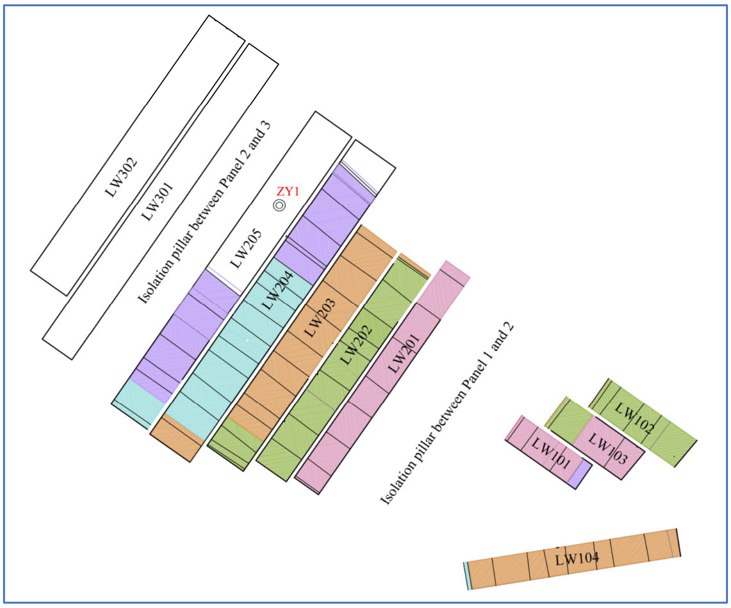

Figure 1. The layout of working faces in the panels.

3. Field Monitoring

In order to master the internal movement law of overlying strata, an observation borehole ZY1 was drilled in the ground surface of LW205 with a depth of 940 m (the layout position is shown in Figure 1). A dual-channel DOFS with a depth of 930 m was arranged inside the borehole (the scheme is shown in Figure 2a), and the on-site installation process is shown in Figure 2b. Meanwhile, a GNSS system was also arranged on the surface to monitor the changes in surface subsidence in real time (Figure 2c).

(**a**) (**b**) (**c**)

Figure 2. The on-site installation and equipment of observation borehole ZY1: (**a**) observation scheme; (**b**) on-site installation; (**c**) monitoring equipment.

After the drilling of observation borehole ZY1 was completed, the corresponding columnar distribution results of strata were obtained by logging in the hole. By means of key stratum discrimination software, the ZY1 column was judged and the key stratum distribution was obtained, as shown in Figure 3. It can be seen from Figure 3 that there are 14 key strata in the whole overburden above the coal seam.

NO.	Depth (m)	Thickness (m)	Lithology	Legend
180	173.15	173.15	Loess	
179	1.75	174.9	Sandy mudstone	
178	3.4	178.3	Siltstone	
177	1.05	179.35	Fine Sandstone	
176	3.3	182.65	Siltstone	
175	0.7	183.35	Sandy mudstone	
174	1.15	184.5	Fine Sandstone	
173	11.95	196.45	Siltstone	PKS
172	1.8	198.25	Mudstone	
171	10.1	208.35	Fine Sandstone	
170	3.75	212.1	Siltstone	
169	1.2	213.3	Fine Sandstone	
168	4.7	218	Siltstone	
167	2	220	Fine Sandstone	
166	4.8	224.8	Sandy mudstone	
165	4.25	229.05	Fine Sandstone	
164	4.15	233.2	Siltstone	
163	2.7	235.9	Sandy mudstone	
162	2.4	238.3	Fine Sandstone	
161	1.25	239.55	Mudstone	
160	2	241.55	Fine Sandstone	
159	1.35	242.9	Siltstone	
158	2.95	245.85	Fine Sandstone	
157	6.75	252.6	Siltstone	
156	2.05	254.65	Fine Sandstone	KS13
155	3.4	258.05	Siltstone	
154	7.85	265.9	Fine Sandstone	
153	2.85	268.75	Sandy mudstone	
152	2	270.75	Fine Sandstone	
151	1.7	272.45	Sandy mudstone	
150	1.9	274.35	Fine Sandstone	
149	2.7	277.05	Mudstone	
148	4.35	281.4	Fine Sandstone	
147	6.35	287.75	Siltstone	
146	2.45	290.2	Fine Sandstone	
145	2.55	292.75	Mudstone	KS12
144	2.9	295.65	Fine Sandstone	
143	9.6	305.25	Sandy mudstone	
142	1.85	307.1	Siltstone	
141	2.4	309.5	Mudstone	
140	1.8	311.3	Fine Sandstone	
139	1.25	312.55	Mudstone	
138	2.05	314.6	Sandy mudstone	
137	3.3	317.9	Fine Sandstone	
136	4.05	321.95	Sandy mudstone	
135	3.65	325.6	Siltstone	
134	5.95	331.55	Sandy mudstone	KS11
133	3	334.55	Mudstone	
132	14.15	348.7	Siltstone	
131	2.95	351.65	Mudstone	
130	1.5	353.15	Siltstone	KS10
129	1.2	354.35	Mudstone	
128	7.9	362.25	Siltstone	
127	1.7	363.95	Mudstone	
126	4	367.95	Fine Sandstone	
125	3.95	371.9	Sandy mudstone	
124	6.8	378.7	Fine Sandstone	
123	2.55	381.25	Mudstone	
122	5.1	386.35	Siltstone	
121	1.2	387.55	Sandy mudstone	
120	7.45	396	Siltstone	
119	1.65	396.65	Mudstone	KS9
118	4.25	400.9	Fine Sandstone	
117	13.45	414.35	Sandy mudstone	
116	1.1	415.45	Fine Sandstone	
115	1.3	416.75	Mudstone	
114	3	419.75	Fine Sandstone	
113	1.05	420.8	Mudstone	
112	1.4	422.2	Fine Sandstone	
111	0.75	422.95	Sandy mudstone	
110	1.1	424.05	Fine Sandstone	
109	1.05	425.1	Mudstone	
108	1.2	426.3	Fine Sandstone	
107	4.95	431.25	Sandy mudstone	
106	1.35	432.6	Siltstone	
105	1.45	434.05	Mudstone	
104	1.15	435.2	Fine Sandstone	
103	0.7	435.9	Sandy mudstone	
102	1.65	437.55	Fine Sandstone	
101	3.7	441.25	Sandy mudstone	
100	0.8	442.05	Fine Sandstone	
99	3.95	446	Sandy mudstone	
98	2.55	448.55	Fine Sandstone	
97	4.4	452.95	Sandy mudstone	
96	4.85	457.8	Fine Sandstone	
95	4.55	462.35	Sandy mudstone	
94	4.7	467.05	Fine Sandstone	
93	3.4	470.45	Mudstone	
92	10	480.45	Fine Sandstone	KS8
91	4.95	485.4	Medium Sandstone	
90	9.95	495.35	Fine Sandstone	

NO.	Depth (m)	Thickness (m)	Lithology	Legend
89	25.3	520.65	Medium sandstone	
88	7.2	527.85	Fine Sandstone	
87	0.85	528.7	Mudstone	
86	12.8	541.5	Fine Sandstone	KS7
85	22.9	564.4	Medium sandstone	
84	25.05	589.45	Coarse sandstone	
83	8.05	597.5	Fine Sandstone	
82	5.65	603.15	Medium sandstone	
81	7	610.15	Gravelly coarse sandstone	
80	3.85	614	Fine Sandstone	
79	1.3	615.3	Siltstone	
78	4.55	619.85	Medium sandstone	
77	1.85	621.7	Fine Sandstone	
76	3	624.7	Medium sandstone	
75	2.4	627.1	Fine Sandstone	
74	4.55	631.65	Medium sandstone	
73	1.25	632.9	Siltstone	
72	10.8	643.7	Fine Sandstone	KS6
71	17.2	660.9	Gravelly medium sandstone	
70	1.15	662.05	Mudstone	
69	4.15	666.2	Fine Sandstone	
68	2.35	668.55	Medium sandstone	
67	9.25	677.8	Fine Sandstone	
66	0.9	678.7	Coarse sandstone	
65	7.95	686.65	Fine Sandstone	
64	1.8	688.45	Medium sandstone	
63	4.1	692.55	Siltstone	
62	3.8	696.35	Coarse sandstone	
61	0.65	697	Mudstone	
60	2.35	699.35	Fine Sandstone	
59	0.8	700.15	Mudstone	
58	2.1	702.25	Fine Sandstone	
57	9.6	711.85	Coarse sandstone	
56	4.85	716.7	Fine Sandstone	
55	6.95	723.65	Medium sandstone	
54	5.4	729.05	Fine Sandstone	
53	1.05	730.1	Medium sandstone	
52	2.15	732.25	Fine Sandstone	
51	3.2	735.45	Medium sandstone	
50	5.35	740.8	Coarse sandstone	
49	0.8	741.6	Mudstone	
48	10.7	752.3	Fine Sandstone	KS5
47	7.3	759.6	Medium sandstone	
46	16	775.6	Fine Sandstone	
45	2.25	777.85	Medium sandstone	
44	5.5	783.35	Siltstone	
43	7.1	790.45	Fine Sandstone	
42	3.75	794.2	Medium sandstone	
41	13.5	807.7	Fine Sandstone	KS4
40	3.7	811.4	Medium sandstone	
39	9.2	820.6	Coarse sandstone	KS3
38	8.45	829.05	Siltstone	
37	12.6	841.65	Fine Sandstone	
36	0.7	842.35	Mudstone	
35	10.7	853.05	Coarse sandstone	KS2
34	2.65	855.7	Mudstone	
33	8.65	864.35	Coarse sandstone	
32	5.1	869.45	Mudstone	
31	0.85	870.3	Fine Sandstone	
30	2.6	872.9	Mudstone	
29	0.65	873.55	Siltstone	
28	1.45	875	Mudstone	
27	1.45	876.45	Medium sandstone	
26	4.2	880.65	Mudstone	KS1
25	1.1	881.75	Medium sandstone	
24	5.5	887.25	Siltstone	
23	1.3	888.55	Mudstone	
22	2.35	890.9	Siltstone	
21	1.15	892.05	Medium sandstone	
20	1.15	893.2	Mudstone	
19	1.85	895.05	Sandy mudstone	
18	0.9	895.95	Fine Sandstone	
17	4.75	900.7	Siltstone	
16	0.85	901.55	Fine Sandstone	
15	1.35	902.9	Sandy mudstone	
14	4.1	907	Coarse sandstone	
13	3.45	910.45	Mudstone	
12	1.35	911.8	Medium sandstone	
11	3.25	915.05	Fine Sandstone	
10	2.8	917.85	Mudstone	
9	5.3	923.15	Medium sandstone	
8	3.1	926.25	Coarse sandstone	
7	4.05	930.3	Fine Sandstone	
6	4.45	934.75	Medium sandstone	
5	3.65	938.4	Fine Sandstone	
4	4.83	943.23	Coarse sandstone	
3	7.7	950.93	Sandy mudstone	
2	4.19	955.12	Siltstone	
1	1.5	956.62	Mudstone	
0	10.26	966.88	Coal seam	

Figure 3. ZY1 column and discrimination results of key strata.

With ZY1 being 292 m ahead of the working face, the installation of DOFS in the borehole and the GNSS monitoring system for surface subsidence was completed on 27 November 2020 and strain measuring was conducted for the first time. From then on, strain measuring was conducted regularly until 26 October 2021, when mining of the working face was over. At that time, the working face had advanced beyond ZY1 by 380.4 m. Even after mining of the working face was over, strain measuring was still conducted many times, and the last measurement was conducted on 6 December 2021. The first strain value measured was set as the benchmark, then the strain data obtained from each subsequent measurement were processed with overall differential processing with the benchmark. The strain difference curves obtained are shown in Figure 4. As can be seen, the negative value in the vertical coordinate indicates that the rock formation is under compressive strain, while the positive value indicates that the rock formation is under tensile strain.

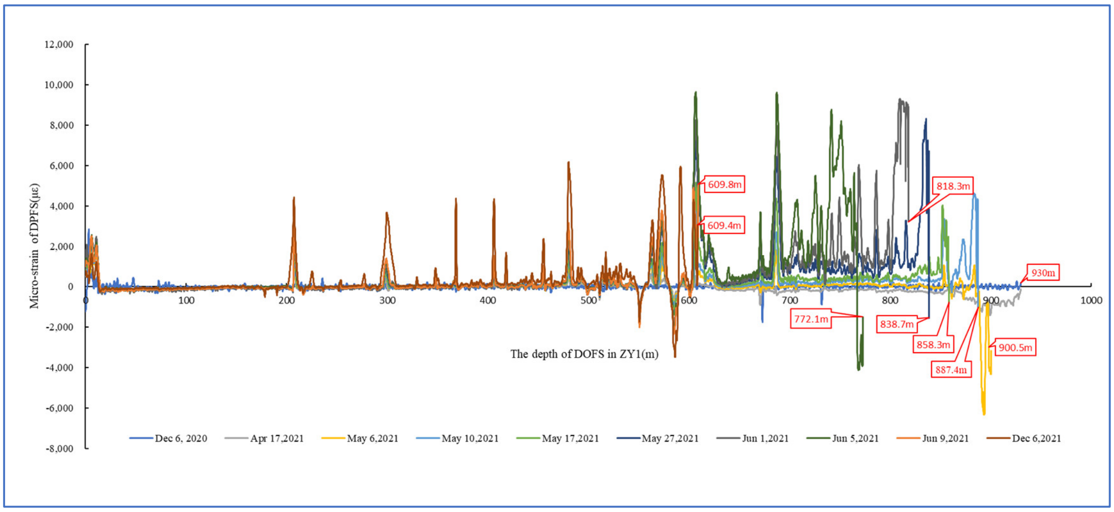

Figure 4. The in situ strain curves of DOFS during the mining process of LW205.

As can be seen from Figure 4, when ZY1 was ahead of the working face (the corresponding mining time was before 10 May 2021), the overlying strata were affected by the advance stress. On 6 May 2021, when ZY1 was 12.6 m ahead of the working face, the DOFS at a depth of 900.5 m in the borehole was broken because the compression was beyond its strain limit.

On 10 May 2021, when the working face advanced past ZY1 by 0.5 m, the strain of the DOFS in the borehole changed from compressive strain to tensile strain and the DOFS broke at the depth of 887.4 m, which corresponded to KS1 in the borehole.

On 17 May 2021, when the working face advanced past ZY1 by 18.4 m, the DOFS broke at the depth of 853.7 m, which corresponded to KS2 in the borehole.

On 27 May 2021, when the working face advanced past ZY1 by 47.6 m, the DOFS broke at the depth of 838.7 m, which corresponded to KS3 in the borehole.

On 1 June 2021, when the working face advanced past ZY1 by 61.3 m, the DOFS broke at the depth of 818.3 m, which corresponded to KS4 in the borehole.

On 5 June 2021, when the working face advanced past ZY1 by 71.3 m, the DOFS broke at the depth of 772.1 m, which corresponded to KS5 in the borehole.

On 9 June 2021, when the working face advanced past ZY1 by 81.5 m, the DOFS broke at the depth of 609.8 m, which corresponded to the range between KS6 and KS7 in the borehole. Since then, as the working face continued to advance, the breakpoint height of the DOFS tended to be stable.

On 26 October 2021, when mining of the working face was over, the working face had advanced past ZY1 by 380.4 m. On 6 December 2021, the strain was measured for the last time, which revealed that the stain value increased slightly but the position of the breakpoint remained unchanged. This indicates that the high overlying strata above KS7 remained in a basically stable state.

In addition to the above regular monitoring of DOFS in the borehole, real-time monitoring of the surface subsidence near the mouth of ZY1 was conducted and the corresponding curve was obtained, as shown in Figure 5. As can be seen, when the working face advanced past ZY1 by 380 m, the corresponding surface subsidence value was approximately 588 mm. Since the mining height of LW205 is 10 m, the corresponding subsidence ratio is about 0.058, indicating that the overlying strata are not broken yet and are in a state of bending deformation.

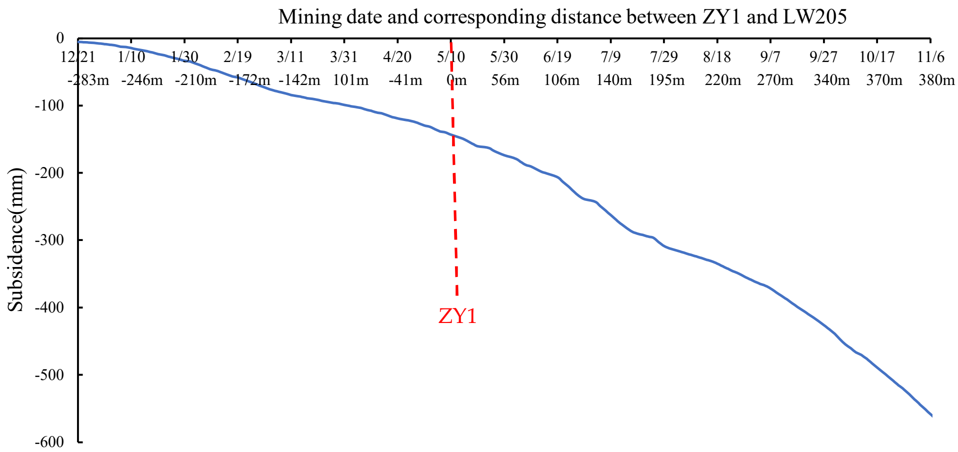

Figure 5. The in situ surface subsidence curve of ZY1 after LW205 mining.

4. Numerical Simulation

4.1. Simulation Schemes

Based on the columnar distribution of rock strata in the three panels and actual geological data, a numerical model was established by using 3DEC discrete element software. By using the discrete element method, the rock mass is treated as blocks which can produce displacement and torsion motion. In this way, 3DEC discrete element software can effectively simulate the phenomena of fracture, separation, deformation, and failure of the surrounding rock. According to the key stratum theory, the key stratum controls the deformation and fracture of the whole overlying rock. Therefore, the key stratum in Figure 3 is retained in the model, while other rock strata are replaced by homogenized soft rock. In order to facilitate the simulations, the strike dimensions of the working face in panel 2 and panel 3 in Figure 1 were uniformly processed, and the plane layout of the working face in the model is shown in Figure 6.

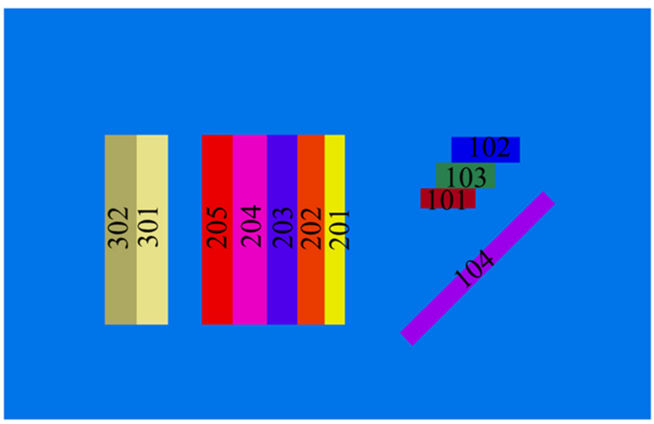

Figure 6. The working face plan of the discrete element model.

A 3D numerical model (4100 m × 2600 m × 500 m) was established (as shown in Figure 7a) to simulate the mining process of three panels and analyze the evolution law of mining-induced stress in the coal seam. The constitutive model for rock in numerical simulations is the Mohr–Coulomb model and the material property is elastoplastic. In the mining process, one working face is excavated each time, and the excavation sequence is as follows: panel 1, panel 2, LW302, and LW301. After the excavation is over, the model will be calculated to reach a state of equilibrium again. In order to conduct a comparative analysis of the influence of key strata on the evolution of mining-induced stress, the block and joint strength of key strata was weakened on the basis of the model in Figure 7a, and a weakened model without key strata was obtained, as shown in Figure 7b.

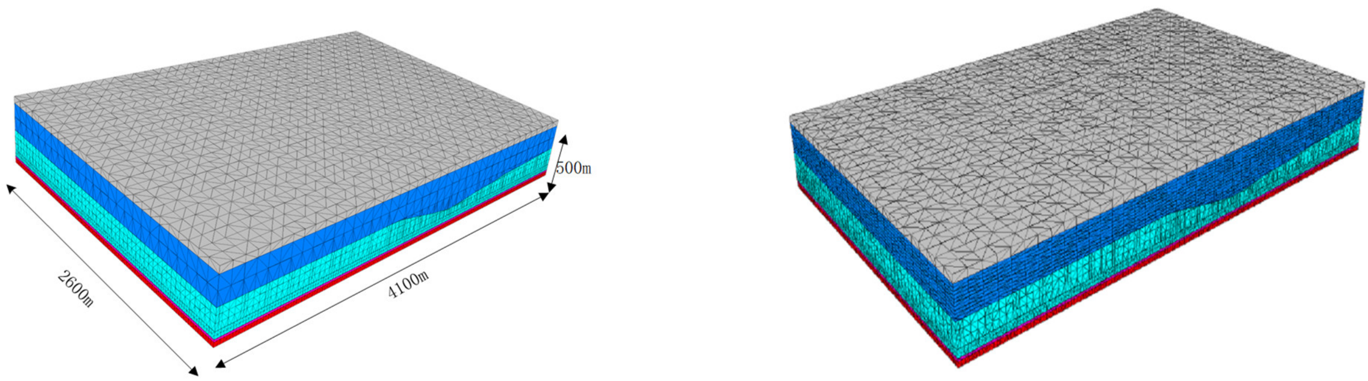

(**a**) (**b**)

Figure 7. The stereogram of three-dimensional discrete element model: (**a**) the actual model; (**b**) the weakened model.

Since the purpose of this study is to obtain the stress evolution law of the surrounding rock and the failure law of roof strata in the mining process, the thickness of the floor in the model is slightly smaller. At the same time, in order to eliminate the boundary effect, a distance of more than 600 m is reserved on both sides of the working face. Given that the burial depth of the working face is nearly one kilometer, in order to facilitate model calculations, the top boundary of the model is constrained by a uniform load on the premise that the simulation results are not to be affected. To be specific, a vertical stress of 13.2 MPa was applied in accordance with the burial depth of the model. Meanwhile, the horizontal and vertical constraints were applied to the surrounding boundary and the bottom boundary, respectively, and their displacement was fixed to 0. Based on the geological histogram of the area under study, the numerical model was built layer by layer from the bottom boundary according to the actual thickness and lithology of the rock (coal) layer. This model design is more complex in structure, but it can simulate the movement of the roof of the coal seam more realistically and accurately.

In order to make the simulation results more aligned with the actual situation, inversion modeling was carried out based on the field measured surface subsidence data. The simulated surface subsidence curve of LW205 after mining in Model 7(a) is shown in Figure 8. When the working face is pushed 380 m past the observation point, the surface subsidence is 590 mm, which is basically consistent with the measured results in Figure 5, indicating that the actual model established is in line with the actual mining conditions, thus ensuring the reliability of subsequent simulation results.

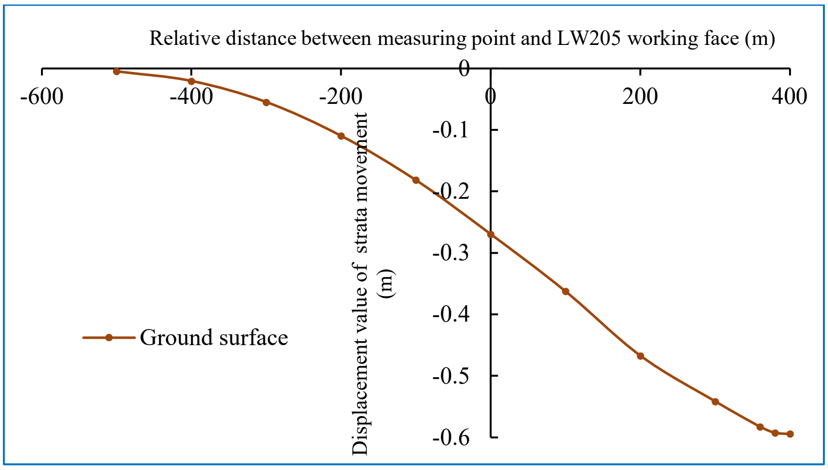

Figure 8. The simulated surface subsidence curve after LW205 mining in the actual model.

4.2. The Evolution Law of Mining-Induced Stress in Panel 1 and Panel 2

With the progress of working face, the equilibrium state of rock mass around the stope is broken and the gravity of the overlying rock strata in the goaf is transferred to the surrounding coal body. Within a certain range around the stope, the vertical stress of the coal seam increases significantly, forming stress concentrations. In the actual mining process, when the working faces of LW201~LW204 were mined, many rock burst accidents occurred in the main roadway in the isolated coal pillar area between panel 1 and panel 2.

In order to analyze the stress distribution of the surrounding rock of the stope in the mining process, the vertical stress distribution cloud map (Figure 9) of the coal seam was derived for analysis after the mining of LW204.

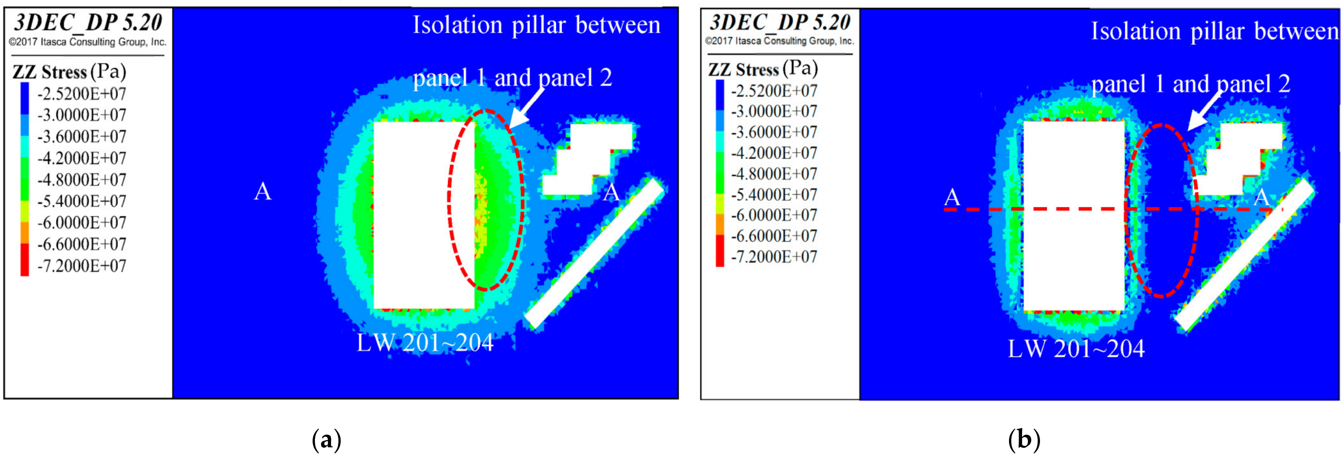

Figure 9. The cloud map of vertical stress distribution in the coal seam after the mining of LW204: (**a**) the actual model; (**b**) the weakened model.

As is shown in Figure 9a, the bearing stress around the goaf increases to a large extent after the working face in the first panel and LW201~204 working faces are mined. Comparatively speaking, the stress increases mildly around the goaf in the first panel, whereas the stress increases significantly in the second panel. Figure 9b shows that the stress increase in the coal pillar area between the first panel and the second panel is not noticeable after the key stratum is weakened.

In order to further explain the distribution law of mining-induced stress in the first and second panels, a measuring line, A-A, was set in the first and second panel to monitor the vertical stress data. The vertical stress curve of LW204 after mining the working face was obtained, as shown in Figure 10.

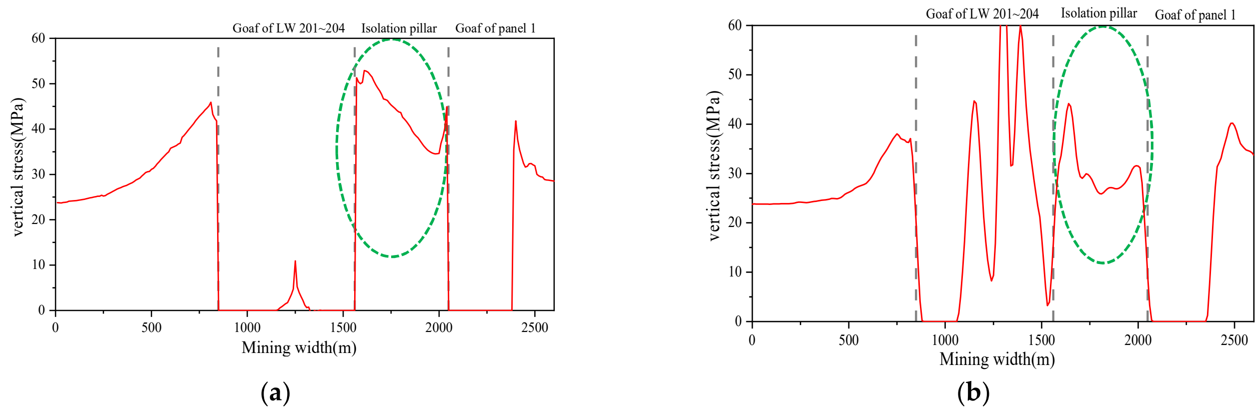

Figure 10. The vertical stress curve in the coal seam after mining of LW204: (**a**) the actual model; (**b**) the weakened model.

As is shown in Figure 10a, when panel 1 and LW201~204 in panel 2 are mined, the vertical stress in the isolated coal pillar area (the green circle area) between panel 1 and panel 2 has a trapezoidal distribution, with one side high and the other side low, and the stress at the edge of the goaf in panel 2 is obviously higher than that at the edge of panel 1. In the isolated coal pillar area between panel 1 and panel 2, the stress increases significantly. The average stress is about 43 MPa and the stress concentration coefficient reaches 1.79. When the key stratum is weakened, the stress increase in the isolated coal pillar area between panel 1 and panel 2 is not obvious (the green circle area as shown in Figure 10b), the average stress in this area is about 32 MPa, and the stress concentration coefficient reaches 1.33.

The above simulation results show that the key stratum existing in the overlying strata has a significant influence on the mining-induced stress evolution of the coal seam. Moreover, the results also reveal the mechanism of rock burst accidents in the main roadway in the isolated coal pillar area between panel 1 and panel 2 after the mining of LW201-204 working faces.

4.3. The Evolution Law of Mining-Induced Stress in Panel 2 and Panel 3

With the increase in the goaf area, the stress of the coal seam around the goaf further increases. Especially when panel 2 is mined, the goaf is virtually one kilometer wide and the whole panel is basically in a full mining state. As the mining continues in panel 3, the stress in the isolated coal pillar area between panel 2 and panel 3 exhibits a significant change. Therefore, the vertical stress distribution cloud map and stress curve of the coal seam were derived for further analysis after LW205 and LW302 are mined. Figures 11 and 12 show the cloud map and stress curve corresponding to the two working faces, respectively.

Theoretically, the stress influence boundary should be divided according to the standard that the bearing stress should be more than 1.05 times the original stress (the green lines as shown in Figure 10c,d). As can be seen from Figure 11, when LW205 in panel 2 is mined, the influence range of the lateral bearing stress is 660 m. However, the influence range of lateral bearing stress in the weakened model is reduced to 400 m.

As can be seen from Figure 12, due to the mining of panel 3, the vertical stress in the isolated coal pillar area between panel 2 and panel 3 rises and, noticeably, a high stress zone is formed. As LW302 is mined, stress is concentrated in the isolated coal pillar area between panel 2 and panel 3 (the green circle area as shown in Figure 12c). The stress in the area is generally over 40 MPa, with the peak value reaching 60.24 MPa and the stress concentration coefficient being as high as 2.51. This indicates that when LW302 is mined, its adjacent working face LW301 is in a state of high stress. In other words, the risk of rock burst is rather high in this mining process. However, in the weakened model, no obvious stress concentration occurs in LW301 and the stress in the central part of the isolated coal pillar area between panel 2 and panel 3 does not increase significantly (the green circle area as shown in Figure 12d).

With the mining of LW301, the stress in the isolated coal pillar area between panel 2 and panel 3 displays a further rising trend. After LW301 reaches a state of equilibrium, the vertical stress distribution cloud map and stress curve of coal seam were derived, as shown in Figure 13.

As is shown in Figure 13a, due to the mining of LW301, the stress in the isolated coal pillar area between panel 2 and panel 3 displays a remarkable rising trend. The maximum stress in the central part of isolated coal pillar area between panel 2 and panel 3 reaches up to 72 MPa, with the stress concentration coefficient being as high as 2.92. This peak value is far higher than the vertical stress in other areas around the goaf in panel 3 (the green circle area as shown in Figure 13a). As can be seen from the green circle area in Figure 13b, when the key stratum is weakened, no obvious high stress zone is observed near the coal pillar side in LW301.

Figure 13c shows that the stress in the coal pillar area increases further after LW301 is mined. The average vertical stress upon the isolated coal pillars between panel 2 and panel 3 increases by 17 MPa. In particular, the stress of LW301′s return airway near the coal pillar side increases by about 30 MPa compared to LW302 after mining. As can be observed in Figure 13d, when the key stratum is weakened, concentrated stress is not obvious in the LW301 return airway. This indicates that due to the influence of the key stratum of the overlying strata, the rock burst risk of the return airway along the coal pillar side is greater in the mining process of LW301. Accordingly, anti-shock and pressure relief measures should be taken in advance to ensure safety during the mining period. As is revealed through field investigations, during the mining process of LW301, several roof-fall events occurred in the return airway, which verifies the correctness of the simulation results.

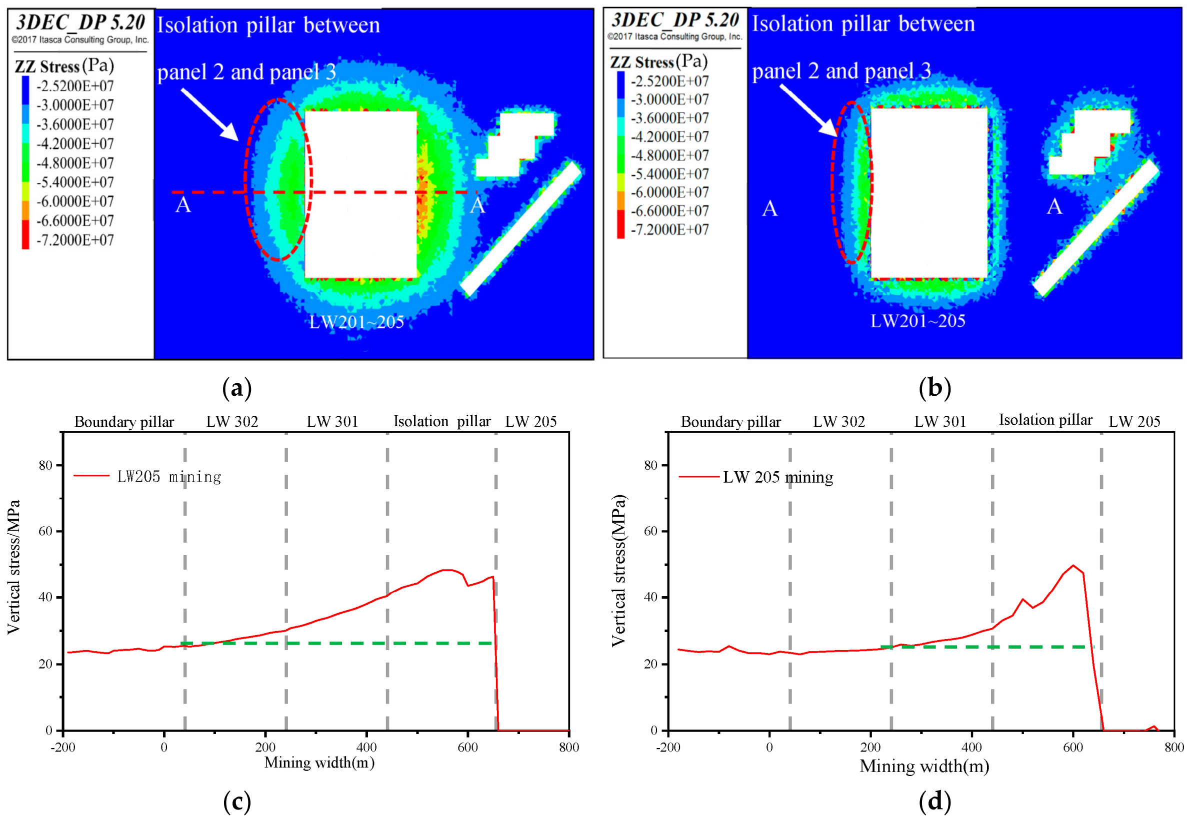

Figure 11. The vertical stress distribution cloud map and stress curve in the coal seam after the mining of LW205: (**a**) the cloud map of the actual model; (**b**) the cloud map of the weakened model; (**c**) the stress curve of the actual model; (**d**) the stress curve of the weakened model.

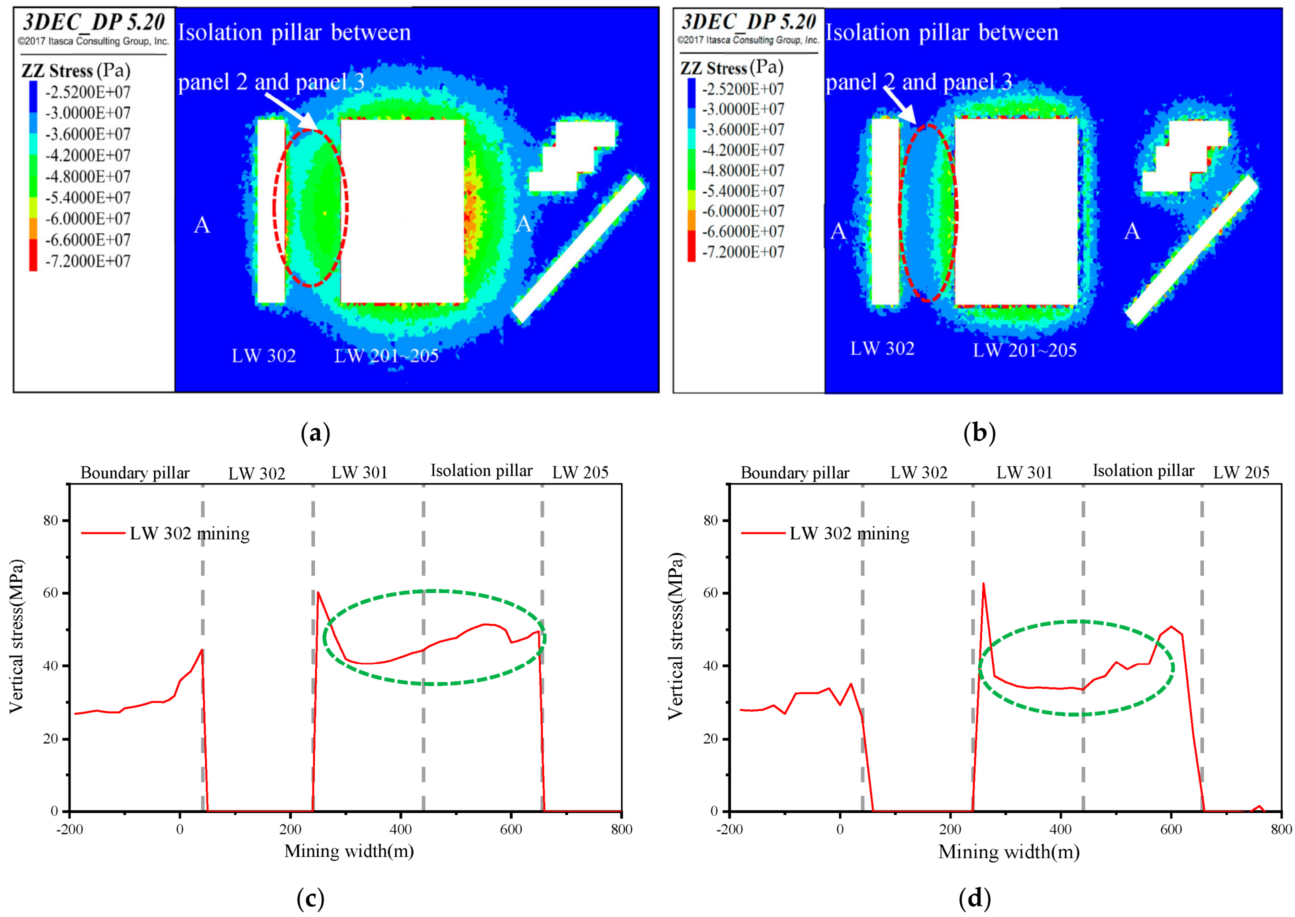

Figure 12. The vertical stress distribution cloud map and stress curve in the coal seam after the mining of LW302: (**a**) the cloud map of the actual model; (**b**) the cloud map of the weakened model; (**c**) the stress curve of the actual model; (**d**) the stress curve of the weakened model.

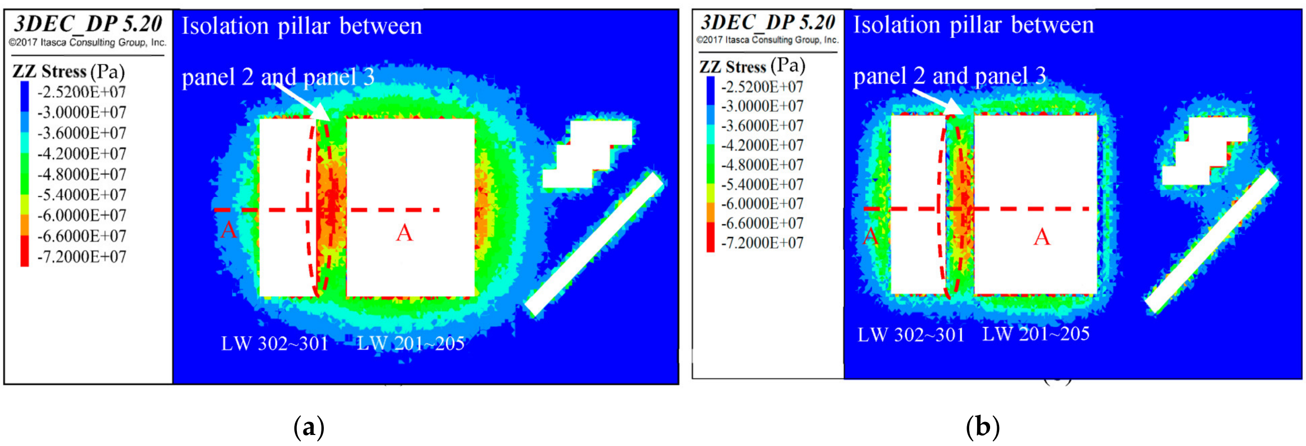

Figure 13. *Cont.*

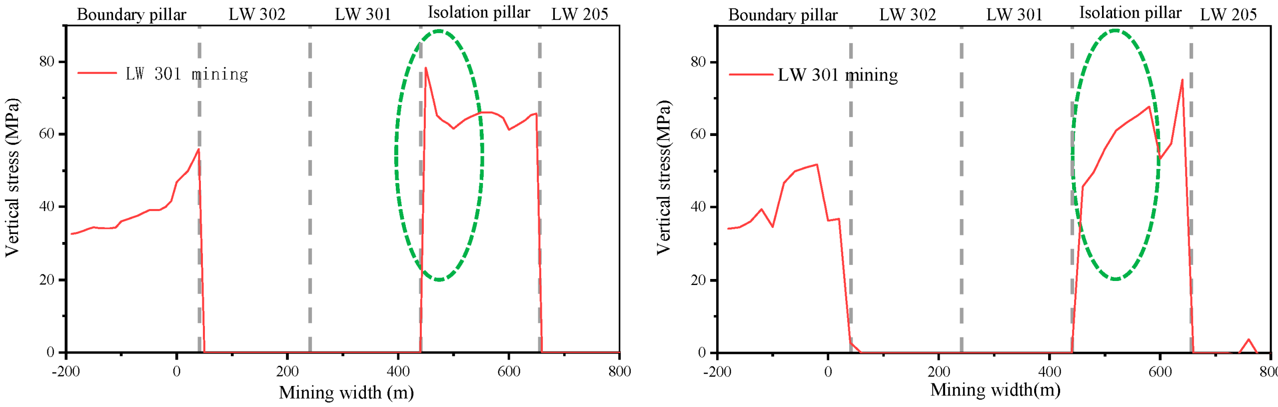

(**c**) (**d**)

Figure 13. The vertical stress distribution cloud map and stress curve in the coal seam after the mining of LW301: (**a**) the cloud map of the actual model; (**b**) the cloud map of the weakened model; (**c**) the stress curve of the actual model; (**d**) the stress curve of the weakened model.

5. Conclusions

1. The ground observation borehole was drilled in the test mine and a DOFS and a surface subsidence GNSS monitoring system were installed inside and at the mouth of the borehole, respectively. According to the monitoring data on strain obtained by the DOFS, the height of the broken stratum in the overlying rock after mining is much lower than that of the main key stratum, indicating that fracture does not occur in the high key strata. As the monitoring results of the GNSS monitoring system show, the surface subsidence volume is 0.058 m and the subsidence coefficient is less than 0.1. This verifies again that the high key strata do not break and enter a state of bending subsidence instead.
2. By comparing the simulation results, it is found that when there are multiple key strata in the overlying strata, the stress concentration in the isolated coal pillar between panel 1 and panel 2 is greatly affected after the mining of LW201–LW204. This reveals the working mechanism of rock burst accidents in the main roadway in the isolated coal pillar area between panel 1 and panel 2.
3. By comparing the simulation results, it is predicted that when there are multiple key strata in the overlying strata, the stress concentration risk in the LW301 return airway along the coal pillar between panel 2 and panel 3 is relatively high compared to LW302 after mining. After actual mining, several roof-fall events occurred in the return airway, which verifies the accuracy of the predicted results.
4. The paper reveals the mechanism of rock burst accidents caused by the significant influence of multiple key strata in the overlying strata on stress concentration in coal seams. Moreover, it predicts the potential hazard areas after mining. The research results are of great guiding significance for the prevention and control of rock burst accidents.

Author Contributions: Conceptualization, J.X. and W.Z.; formal analysis, J.X. and S.N.; writing—original draft preparation, J.X. and S.N.; writing—review and editing, W.Z. and X.W.; investigation, J.X. and T.H.; validation, W.Z. and X.W. All authors have read and agreed to the published version of the manuscript.

Funding: National Natural Science Foundation of China (52274097). The project was also funded by Shaanxi Zhengtong Coal Industry Co., Ltd., Shandong Energy, China.

Institutional Review Board Statement: Not applicable.

Informed Consent Statement: Not applicable.

Data Availability Statement: The data presented in this study are available on request from the corresponding author.

Acknowledgments: We extended our sincere thanks to the relevant staff at the State Key Laboratory of Coal Exploration and Intelligent Mining for the simulation experiments.

Conflicts of Interest: The authors declare no conflict of interest.

References

1. Qian, M.G.; Miao, X.X.; Xu, J.L. Theoretical study of key stratum in ground control. *J. Chin. Coal Soc.* **1996**, *21*, 225–230.
2. Xie, J.L.; Xu, J.L.; Wang, F. Mining-induced stress distribution of the working face in a kilometerdeep coal mine—A case study in Tangshan coal mine. *J. Geophys. Eng.* **2018**, *15*, 2060–2070. [CrossRef]
3. Xie, J.L.; Xu, J.L. Effect of key stratum on the mining abutment pressure of a coal seam. *Geosci. J.* **2017**, *21*, 267–276. [CrossRef]
4. Liu, H.; Yu, B.; Liu, J.R.; Wang, T.X. Investigation of impact rock burst induced by energy released from hard rock fractures. *Arab. J. Geosci.* **2019**, *12*, 381. [CrossRef]
5. Guo, W.H.; Cao, A.Y.; Xue, C.C.; Hu, Y.; Wang, S.W.; Zhao, Q. Mechanism and evolution control of wide coal pillar bursts in multithick key strata. *Shock Vib.* **2021**, *2021*, 4696619. [CrossRef]
6. Yang, Z.Q.; Liu, C.; Zhu, H.Z.; Xie, F.X.; Dou, L.M.; Chen, J.H. Mechanism of rock burst caused by fracture of key strata during irregular working face mining and its prevention methods. *Int. J. Rock Mech. Min.* **2019**, *29*, 889–897. [CrossRef]
7. Zhu, Z.J.; Wu, Y.L.; Han, J.; Chen, E. Overburden failure and ground pressure behaviour of longwall top coal caving in hard multi-layerd roof. *Arch. Min. Sci.* **2019**, *64*, 575–590.
8. Tahmasebinia, F.; Zhang, C.G.; Canbulat, I.; Sepasgozar, S.; Saydam, S. A novel damage model for strata layers and coal mass. *Energies* **2020**, *13*, 1928. [CrossRef]
9. Jiang, L.S.; Wu, Q.S.; Wu, Q.L.; Wang, P.; Xue, Y.C.; Kong, P.; Gong, B. Fracture failure analysis of hard and thick key layer and its dynamic response characteristics. *Eng. Fail. Anal.* **2019**, *98*, 118–130. [CrossRef]
10. Zhang, J.G.; Yang, W.; Lin, B.Q.; Zhang, J.J.; Wang, M. Strata movement and stress evolution when mining two overlapping panels affected by hard stratum. *Int. J. Rock Mech. Min.* **2019**, *29*, 691–699. [CrossRef]
11. Ning, S.; Zhu, W.B.; Xie, J.L.; Song, S.K.; Wang, X.Z.; Yu, D.; Lou, J.F.; Xu, J.L. Influence of stress distribution in coal seams of non-uniform extremely thick key stratum and disaster-causing mechanisms. *Sci. Rep.* **2022**, *12*, 14465. [CrossRef] [PubMed]
12. Zhang, M.; Hu, X.L.; Huang, H.T.; Chen, G.Y.; Gao, S.; Liu, C.; Tian, L.H. Mechanism and prevention and control of mine earthquake in thick and hard rock strata considering the horizontal stress evolution of stope. *Shock Vib.* **2021**, *2021*, 6680928. [CrossRef]
13. Lv, X.F.; Zhou, H.Y.; Wang, A.W.; Feng, C.; Xiao, X.C. Characteristics of stress transfer and progressive fracture in overlying strata due to mining-induced disturbances. *Adv. Civ. Eng.* **2018**, *2018*, 8967010. [CrossRef]
14. Zhang, T.; Gan, Q.; Zhao, Y.X.; Zhu, G.P.; Nie, X.D.; Yang, K.; Li, J.Z. Investigations into mining-induced stress-fracture-seepage field coupling effect considering the response of key stratum and composite aquifer. *Rock Mech. Rock Eng.* **2019**, *52*, 4017–4031. [CrossRef]
15. Suchowerska, A.M.; Merifield, R.S.; Carter, J.P. Vertical stress changes in multi-seam mining under supercritical longwall panels. *Int. J. Rock Mech. Min.* **2013**, *61*, 306–320. [CrossRef]
16. Yavuz, H. An estimation method for cover pressure re-establishment distance and pressure distribution in the goaf of longwall coal mines. *Int. J. Rock Mech. Min.* **2004**, *41*, 193–205. [CrossRef]
17. Jirankova, E.; Petros, V.; Sancer, J. The assessment of stress in an exploited rock mass based on the disturbance of the rigid overlying strata. *Int. J. Rock Mech. Min.* **2012**, *50*, 77–82. [CrossRef]
18. Liu, W.R. Experimental and numerical study of rock stratum movement characteristics in longwall mining. *Shock Vib.* **2019**, *2019*, 5041536. [CrossRef]
19. Zhang, G.J.; Wang, Z.Y.; Guo, G.L.; Wei, W.; Wang, F.G.; Zhong, L.L.; Gong, Y.Q. Study on regional strata movement during deep mining of Erdos coal field and its control. *Int. J. Environ. Res. Public Health* **2022**, *19*, 14902. [CrossRef] [PubMed]